Enhancements to velocity-dependent dark matter interactions from tidal streams and shells in the Andromeda galaxy

Robyn E. Sanderson, Roya Mohayaee, Joe Silk

Monthly Notices
of the
ROYAL ASTRONOMICAL SOCIETY

Mon. Not. R. Astron. Soc. **420,** 2445–2456 (2012) doi:10.1111/j.1365-2966.2011.20215.x

Enhancements to velocity-dependent dark matter interactions from tidal streams and shells in the Andromeda galaxy

Robyn E. Sanderson,[1⋆] Roya Mohayaee[2] and Joe Silk[2,3]

[1] *Kapteyn Astronomical Institute, PO Box 800, 9700 AV Groningen, the Netherlands*
[2] *UPMC, CNRS, Institut d'Astrophysique de Paris, 98 bis Bd. Arago, Paris 75014, France*
[3] *Physics Department, University of Oxford, Oxford OX1 3RH*

Accepted 2011 November 15. Received 2011 November 8; in original form 2011 June 21

ABSTRACT

Dark matter substructures around nearby galaxies provide an interesting opportunity for confusion-free indirect detection of dark matter. We calculate the boost over a smooth background distribution of dark matter for gamma-ray emission from dark matter self-annihilations in tidal structures in M31, assuming a cross-section inversely proportional to the relative velocities of the dark matter particles as proposed by the Sommerfeld effect. The low velocity of the material in the structure results in a significant increase in gamma-ray emission compared to both the background halo and the predicted emission for a velocity-independent cross-section. We also calculate the expected signal for *Fermi*, for reasonable choices of the dark matter parameters. We find that for a cross-section proportional to v^{-2}, the enhancement to the annihilation rate is sufficient to test the velocity dependence of the cross-section by spatial correlation with the stellar component of the M31 Giant Stream, given sufficient detector sensitivity.

Key words: astroparticle physics – galaxies: individual: M31 – galaxies: kinematics and dynamics – dark matter – gamma-rays: galaxies.

1 INTRODUCTION

Like our own Galaxy, the nearby Andromeda galaxy (M31) exhibits a wealth of stellar features with an accretion origin, including dwarf galaxies, tidal streams, and a complex outer halo structure (McConnachie et al. 2009). Unlike our Galaxy, however, we view M31 from the outside, which in some cases facilitates the study of these substructures. Many of these tidal features are potential tracers of collisionless dark matter associated with their progenitors, which undergoes similar dynamics to stars. These features usually have distinctive, asymmetric shapes at large radii from the centre of their host. This paper considers whether dark matter in tidal structures in M31 could provide a possible indirect detection by ultrasensitive gamma-ray observations in a confusion-free region around this nearby galaxy.

One particularly prominent feature around Andromeda is a giant tidal stream that extends nearly radially away from the centre of M31, commonly known as the 'Giant Stream'. This feature was first observed by Ibata et al. (2001) and has since been studied in great detail. An *N*-body model of the stream by Fardal et al. (2006) has tentatively connected this stream with two other tidal features closer to M31's disc, known as the west and north-east 'shelves' because of a relatively abrupt drop in surface brightness at their edges (Fig. 1, left-hand panel and top right-hand panel). If the three features were all indeed produced in the same minor merger, the extremely high eccentricity required for the orbit of the progenitor implies that the 'shelves' are in fact radial fold catastrophes, otherwise known as caustics. This theory explains the sharp edges of the shells as the point where infalling and outgoing streams of material stripped from the progenitor pass each other near the outer radial turning point of their orbits. Since the motion is nearly radial, the projection of phase space into the r–v_r plane (Fig. 1, bottom right-hand panel) contains nearly all the information about the dynamics of material in the stream and shells. A caustic occurs at each point where the phase-space stream becomes vertical in this projection, and the various features can thus be placed in chronological order of formation. This theory also predicts that near the edge of each shelf, the density will be significantly enhanced, as particles 'pile up' near the radial turning points of their orbits.

Inferring the phase-space distribution of the material in the shells and stream from this *N*-body model also reveals that the relative velocity of material in the features is extremely low, especially in the tidal stream and the very edges of the two caustics (Fig. 2). At the caustic surface and in the stream, the local relative velocities can be less than 10 km s^{-1} (Table 1). This is a result of the increasing thinness of the stream in phase space as time passes, an effect sometimes known as 'gravitational cooling' (Mohayaee & Shandarin 2006).

Features of this type, though expected to be fairly common, are as difficult to detect in the Milky Way as they are straightforward to find in sufficiently deep images of external galaxies. The sharp-edged

⋆E-mail: sanderson@astro.rug.nl

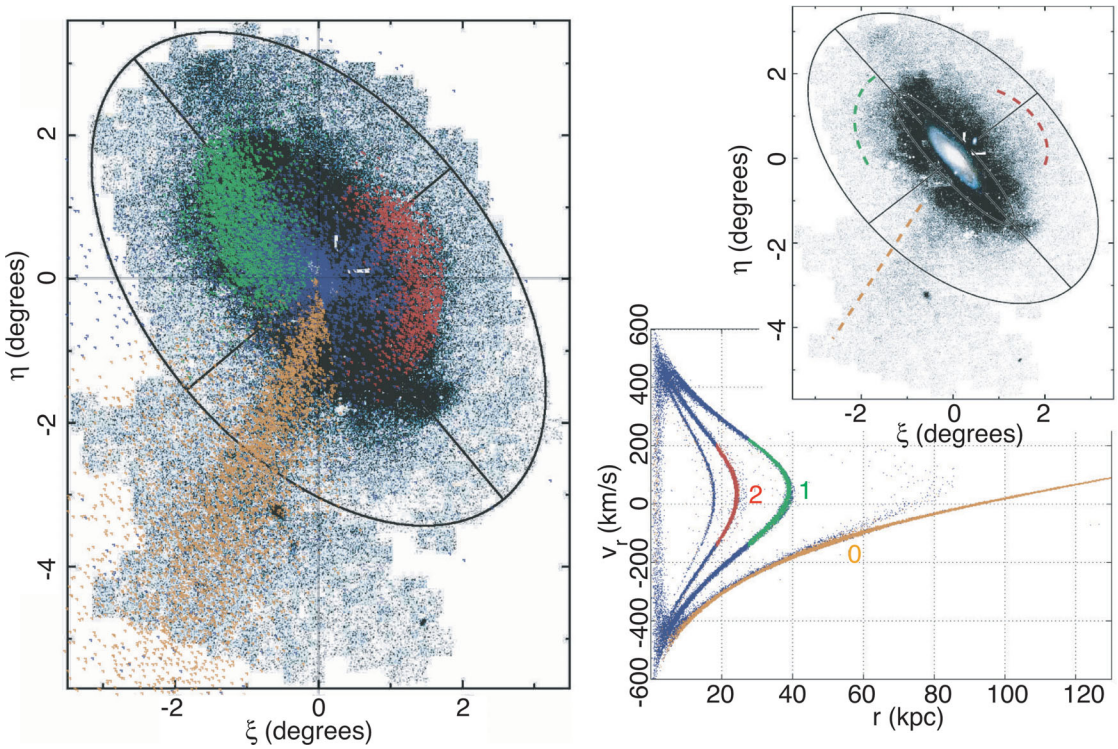

Figure 1. Two tidal features noted around the Andromeda galaxy (left-hand panels, green and red points; top right-hand panel, green and red dashed lines) correspond to fold catastrophes, or caustics, in individual phase wraps of material from a dissolved satellite galaxy on a nearly radial orbit (bottom right-hand panel). For this reason, we refer to the shells in this work as Caustic 1 (green) and Caustic 2 (red), in the order in which they were formed. Another prominent tidal feature, the Giant Stream shown in orange, is the first structure to form in the merger, and hence is labelled '0'.

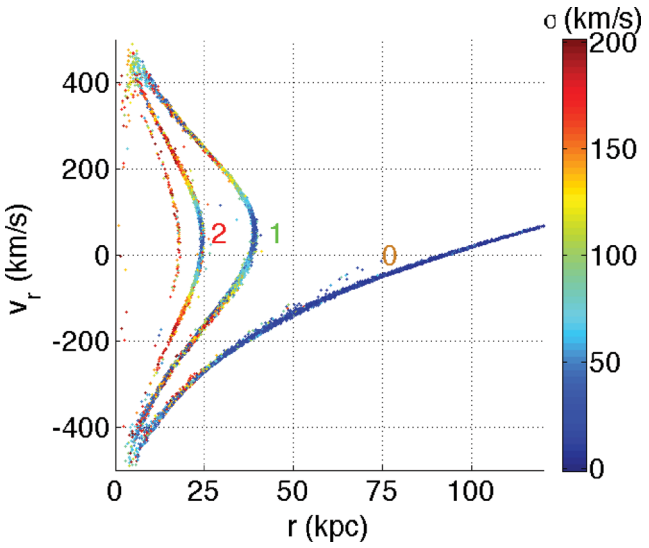

Figure 2. Projected phase-space plot of the tidal debris with $\sigma < 200$ km s^{-1}, colour-coded by the local velocity dispersion estimated from the N-body model (estimation method described in Section 2). The cut in velocity dispersion excludes mainly material near the centre of the halo. The coldest material is found at the edges of the shells and in the tidal tail. For display purposes, a random selection of one-tenth of the particles are plotted here.

Table 1. Mean and minimum estimated velocity dispersions in the features shown in Fig. 1.

Feature (colour in Fig. 1)	$\langle E(\sigma)\rangle$ (km s^{-1})	min$(E(\sigma))$ (km s^{-1})	N_p
Giant Stream 0 (orange)	24	3.6	41 842
Caustic 1 (green)	70	7.3	29 547
Caustic 2 (red)	84	18	12 263

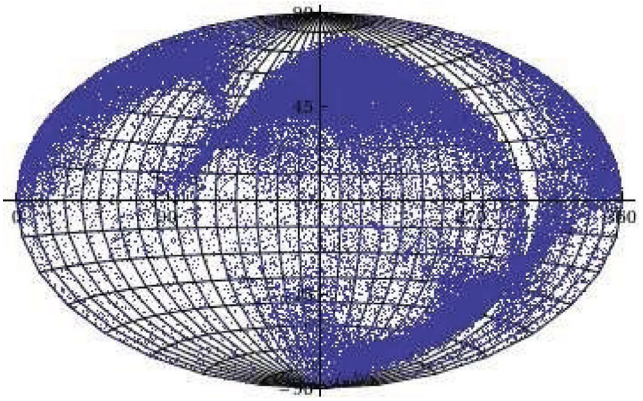

Figure 3. The N-body model of the tidal shells in M31, now viewed in Aitoff projection from a viewpoint at M31's centre. From this perspective, the shells' sharp edges are virtually indistinguishable.

shells seen in the star-count map of M31 would, when viewed from within Andromeda, look instead like large amorphous clouds spread over a huge fraction of the sky (Fig. 3). From this vantage point, much more information about the phase-space structure of the debris would be necessary to determine that the shells existed, whereas when viewed externally in a suitable projection the sharp edges immediately imply a nearly radial orbit for the progenitor. Thus, the existence of such a structure in M31 represents a unique opportunity to study a system with well-constrained dynamics, thanks to its

distinctive morphology as viewed from outside, at the closest range possible without full six-dimensional phase-space information for stars in the shells.

The existence of cold, high-density regions at large radii from M31's centre makes the tidal features an interesting candidate for indirect detection of dark matter in the Sommerfeld enhancement framework, where the interaction probability is boosted at low velocities. The Sommerfeld effect was first introduced to boost the dark matter annihilation signal in order to account for the *PAMELA* observations of positrons and *HESS* and *Fermi* observations of an unpredicted high-energy lepton component in the cosmic rays (Arkani-Hamed et al. 2009; Lattanzi & Silk 2009; March-Russell & West 2009; Cirelli & Cline 2010). The annihilations of a TeV supersymmetric weakly interacting massive particle can be boosted by a factor of the order of 1000, as needed to account for the observed signal. This interpretation has been criticized on several grounds. Excessive gamma-rays (inverse Compton) and high-energy antiprotons would be produced in the inner Galaxy and excessive radio synchrotron emission in the outer Galaxy if the local cold substructure persists at all Galactic radii (Borriello, Cuoco & Miele 2009). The weakness in this critique is that the substructure is likely to be a strong function of Galactic radius. Decrease in substructure concentration factor at large Galactic radii and the effectiveness of tidal disruption at small Galactic radii weaken these constraints significantly. Slatyer, Toro & Weiner (2011) have systematically explored this effect, and conclude that our uncertainty about the radial dependence of the substructure contribution means that no strong constraints can be drawn from comparing signals at different Galactic radii. Any additional information about the expected size of this contribution is therefore quite important for determining the viability of the Sommerfeld model.

The strongest constraint on Sommerfeld boosting has come from considerations of delayed recombination of the Universe following the last scatterings of the cosmic microwave background radiation at $z \sim 1000$. The survival of the model appears marginal for *WMAP* constraints, and *Planck* will soon greatly improve these limits (Galli et al. 2009). However, if the contribution of substructures to the local signal dominates, then these constraints are significantly weakened (Slatyer et al. 2011). Additionally, this line of argument assumes that Sommerfeld boosting, quenched at the local value required to account for *PAMELA*, *HESS* and *Fermi* observations, applies in a regime where the dark matter is much colder ($\beta \equiv v/c \sim 10^{-12}$) than in the local halo substructure where $\beta \sim 10^{-4}$. This is a huge extrapolation that may not necessarily be justifiable in terms of general particle physics models. We believe it is important to test Sommerfeld boosting in a regime much closer to the local environment, for example, in our Galaxy, in ultrafaint dwarf galaxies, and in M31.

Substructures in M31 can provide precisely such a test if we use old stars as dark matter tracers. The proposed test involves *Fermi* imaging of very similar substructures (at least in terms of velocity dispersion) to those invoked locally for the *PAMELA* excess. Without the Sommerfeld enhancement, the material is insufficiently dense to produce a detectable signal (Sanderson & Bertschinger 2010), but with the enhancement signals can be boosted by a factor of up to 10^4–10^5 at velocities comparable to those achieved in the tidal debris in this example. These boost factors are similar to those expected from local dwarf galaxies (Robertson & Zentner 2009). With this in mind, we calculate in this work the boost and signal in the *Fermi* band from this tidal substructure assuming that a dark matter component of the unbound substructure follows the stellar component, as an example of the kind of result one might expect from tidal debris for this class of dark matter models. This particular example has then the additional advantage of a distinctive morphology that could allow it to be easily differentiated from a smooth dark matter halo. It also occupies an interesting niche between the bound substructures thought to dominate the signal in the Milky Way's outer halo and the more diffuse tidally disrupted substructure that Slatyer et al. propose contributes to the extragalactic gamma-ray background. In Section 2, we describe the method by which the phase-space distribution in M31's halo and tidal substructure was modelled, and the results of tests for possible bias in our numerical methods. In Section 3, we present results for the boost factor over the smooth halo as a result of the tidal substructure for different regimes of Sommerfeld boosting. In Section 4, we present maps of the flux in the *Fermi* band for two choices of dark matter model and show how those results may be scaled to other parameter choices. In Sections 5 and 6, we discuss the results and indicate paths for future work.

2 MODELLING

The rate Γ at which dark matter self-annihilations occur is proportional to the volume integral of the total squared number density of dark matter $n_{\rm tot}^2$, weighted by some function $S(v)$ of the relative velocity of particles whose form depends on the class of theories being considered. In our model, there are two distinct density distributions that contribute to the total density: the smooth halo distribution $n_{\rm h}$ and the tidal structure $n_{\rm s}$. The total rate can thus be separated into three different contributions for ease of calculation: one from interactions between dark matter particles in the smooth halo (denoted by a subscript 'hh'), one from dark matter in the tidal structure interacting with dark matter in the smooth halo (denoted by a subscript 'hs'), and one from dark matter particles in the tidal structure interacting with each other (denoted by a subscript 'ss'):

$$\begin{aligned}\Gamma_{\rm tot} &= \int n_{\rm tot}^2 S(v) {\rm d}V, \\ &= \int n_{\rm h}^2 S(\sigma_{\rm h}) {\rm d}V + 2\int n_{\rm h} n_{\rm s} S(v_{\rm s}) {\rm d}V + \int n_{\rm s}^2 S(\sigma_{\rm s}) {\rm d}V, \\ &\equiv \Gamma_{\rm hh} + \Gamma_{\rm hs} + \Gamma_{\rm ss}.\end{aligned} \quad (1)$$

Here we have suppressed the position dependence of the arguments for brevity, and denoted the volume element by dV. The argument to $S(v)$ varies for these three terms. For $\Gamma_{\rm hh}$, the correct relative velocity is the velocity dispersion $\sigma_{\rm h}$ of the halo. For $\Gamma_{\rm hs}$, the halo is assumed to have zero mean velocity relative to the debris, so the mean velocity $v_{\rm s}$ of shell particles is used. For $\Gamma_{\rm ss}$, the velocity dispersion of particles in the tidal debris, $\sigma_{\rm s}$, is used. The shells and tail have such a low velocity dispersion that this last term is anticipated to dominate.

To represent the phase-space distribution of the material in the tidal shells, we used the N-body model constructed by Fardal et al. (2006, 2007) to match the stellar component of the tidal debris. We assumed that the dark component tracks the stellar component and is of equal mass. These assumptions are admittedly an oversimplification but provide a good starting point for two reasons. First, the dark matter components of dwarf galaxies are thought to be more extended and less concentrated than the stellar component (Peñarrubia, Navarro & McConnachie 2008b) but the starting conditions for the N-body model locate the satellite deep in the potential of M31, by which point this extended dark halo would have been tidally stripped already, leaving only the dark matter within a tidal radius consistent with the stellar extent of the satellite. Within

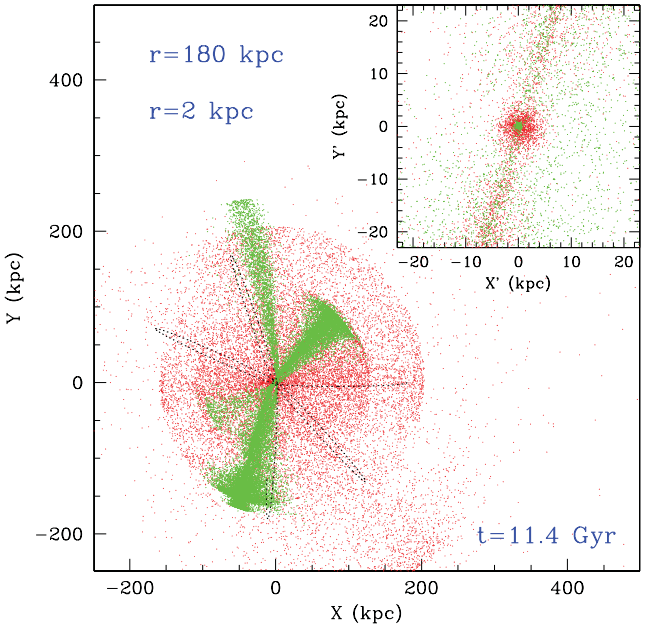

Figure 4. A recent simulation of a satellite falling into a Milky Way type galaxy (see Peñarrubia et al. 2008c, for details of the simulation), showing the creation of shells of both stars (green) and dark matter (red) in a minor merger with a nearly radial initial orbit. The figure shows that star shells trace very closely the dark matter shells and despite the difference in initial distribution, the dark matter and star shells are at similar radii. The inset is a zoom on the satellite which is extremely resilient to the tides.

this radius, the dark matter is thought to contribute roughly equally with the stellar component to the potential of dwarf galaxies, providing some support for assuming comparable masses for the two components. This particular *N*-body model admits a dark matter component up to two to three times the total stellar mass (Fardal, private communication). Secondly, given the similar initial conditions of the stars and dark matter, the stellar shells can provide a visible starting point and template for searches because the radii of the shells, though perhaps not identical, will be similar. A justification for this is seen in simulations that follow both dark and stellar components of a nearly radial merger, as shown in Fig. 4 (see Peñarrubia, Navarro & McConnachie 2008a,c, for full details of the simulations). The star shells, although formed well after the formation of the dark matter shells, clearly trace the dark matter shells and form at similar radii.

2.1 Smooth halo background

The halo used to model the tidal structure was also used to calculate both the smooth background signal and the signal from interaction between dark matter in the halo and putative dark matter in the tidal shells. To make the *N*-body model, only the density profile $\rho(r)$ was necessary (Geehan et al. 2006); it is represented by the NFW relation (Navarro, Frenk & White 1996) with scale radius $r_{\rm h}$ and scale density $\rho_{\rm h,0}$, with the addition of a small core radius $r_{\rm core}$ to produce a finite central density:

$$\rho_{\rm h}(r) = \frac{\rho_{\rm h,0}}{[(r + r_{\rm core})/r_{\rm h}][1 + (r + r_{\rm core})/r_{\rm h}]^2}, \quad (2)$$

as shown in the left-hand panel of Fig. 5. Note that this halo, used consistently for both the dark matter annihilation background and the *N*-body model, has a concentration of $c = 25.5$. This value is significantly higher than the concentration of a typical simulated, M31-sized dark halo grown from cosmological initial conditions, which in most cases is in the range 8–16 (Navarro et al. 2010). This high concentration is a byproduct of the dynamical model and relates to the uncertainty in the mass of M31's disc (the so-called 'disc–halo degeneracy'); in this work, it has the additional effect of producing a larger than usual background signal from the smooth halo density distribution in the innermost regions of the halo.

The velocity dispersion $\sigma(r)$ of the halo was inferred by analogy with the high-resolution numerical studies of the phase-space structure of cosmological haloes by Navarro et al. (2010). These studies confirmed the pseudo-phase-space-density scaling relation $\rho/\sigma^3 \propto r^{-15/8}$, proposed by Bertschinger (1985) as a universal relation for cosmological dark matter haloes, over more than four orders of magnitude in radius. The density profile of the halo was used to determine the radial profile of the velocity dispersion in the halo, scaled to a maximum velocity dispersion determined by rescaling one of the haloes studied in Navarro et al. The average mean velocity of particles in the halo is assumed to be zero, and the resulting

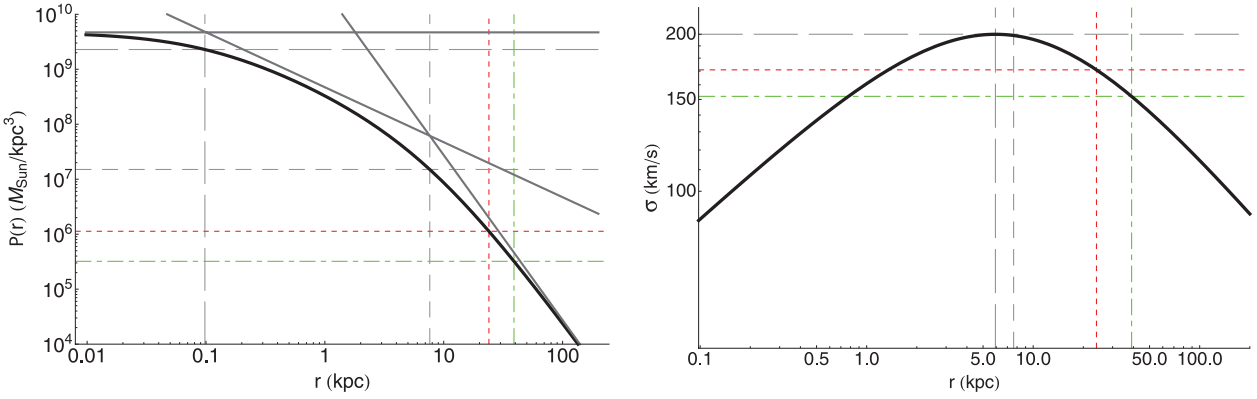

Figure 5. Left-hand panel: density profile of the smooth dark matter halo used in this work. The grey solid lines highlight regions where the power-law index is −3 (at large radius), −1 (at intermediate radius) and 0 (at small radius). The long-dashed lines indicate $r_{\rm core}$, the short-dashed lines indicate $r_{\rm h}$, and the dot–dashed (green online) and dotted (red online) solid lines are the approximate radii of Caustics 1 and 2, respectively. Right-hand panel: velocity dispersion profile of the halo used in this work (solid black line). The profile peaks at $r_{\rm max}$ (long-dashed line), which is just less than the scale radius $r_{\rm h}$ (short-dashed line). The velocity dispersion of halo material in the region of the two caustics (noted as in the left-hand panel) is more than 10 times larger than the velocity dispersion of material in the caustics.

velocity dispersion profile is

$$\sigma_{\rm h}(r) = \sigma_{\rm max}\left(\frac{\rho(r)}{\rho_{\rm max}}\right)^{1/3}\left(\frac{r}{r_{\rm max}}\right)^{5/8}, \tag{3}$$

where it can be shown that

$$r_{\rm max} = \frac{7}{9}r_{\rm h} \qquad \text{and} \qquad \rho_{\rm max} = \frac{729}{1792}\rho_{\rm h} \approx 0.41\rho_{\rm h}. \tag{4}$$

The velocity dispersion profile is shown in the right-hand panel of Fig. 5.

Using the analytic expressions for ρ and σ, we then compute the quantity $\Gamma_{\rm hh}$ analytically:

$$\Gamma_{\rm hh} = \frac{1}{m_{\rm p}^2}\int {\rm d}V\,\rho_{\rm h}^2 S(\sigma_{\rm h}) \tag{5}$$

with $\rho_{\rm h}$ given by equation (2) and $\sigma_{\rm h}$ given by equation (3). For consistency with the N-body model, we normalize the expression to the number density of N-body particles by dividing by $m_{\rm p}^2$. The integral in equation (5) could be taken over the entire volume of the simulation to estimate the total halo flux, but this value depends very strongly on the choice of a core radius for the halo, which is not constrained by the dynamical model. This sensitivity, however, is confined to a tiny region right at the centre of the halo, equivalent to the central 4 pixels or so for *Fermi*. To avoid the strong dependence on a parameter that is so ill-constrained, we instead compare the signal from the halo to that from the tidal structure pixel by pixel over the field. Equation (5) is evaluated for each pixel separately over the entire line of sight (z) and an area on the sky (Δx, Δy) corresponding to the resolution of *Fermi* (about 0.°1, or about 1.4 kpc at the distance of M31). The boost is calculated by comparing the signal in each pixel from the halo and tidal structure. The uncertainty about the core radius leads to unreliable estimates of the boost only for the central few pixels, while the region of interest is at larger radii where the mass profile is somewhat better constrained, and where the boost factor does not depend so strongly on the slope of the mass profile.

2.2 Tidal structure

The tidal structure, including two shells and the Giant Stream, is represented by an N-body realization based on the model constructed by Fardal et al. (2007). Although this model is by no means the single best fit to the available data, it is at least a local best fit that provides a plausible dynamical origin for the debris and a valuable tool for inferring the phase-space structure. Numerical methods are necessary to estimate the signal from the tidal structure; here, we describe these methods and their limitations.

The integrated squared density, weighted by a factor of either $1/v$ or $1/v^2$, was estimated using the optimal procedure identified in Sanderson & Bertschinger (2010), with the addition of estimates for the mean velocity (used to account for interactions between shell and halo dark matter particles) and the velocity dispersion for material in the shell.

Moments of the velocity are calculated as follows. First, the mean velocity $\boldsymbol{v}$ at the centre of the current Riemann volume, located at position $\boldsymbol{x}$, is estimated using

$$\hat{\boldsymbol{v}}(\boldsymbol{x}) = \frac{1}{N_{\rm s}}\sum_{n=1}^{N_{\rm s}}\boldsymbol{v}_n. \tag{6}$$

Here and in the following, the hat symbol indicates an estimator that recovers a smoothed field from the discrete N-body representation. The average relative speed $v_{\rm s}(\boldsymbol{x})$ is then calculated by taking the magnitude of the mean velocity vector:

$$\hat{v}_{\rm s}(\boldsymbol{x}) = \sqrt{\hat{\boldsymbol{v}}\cdot\hat{\boldsymbol{v}}}. \tag{7}$$

The quantity $v_{\rm s}(\boldsymbol{x})$ represents the relative velocity between material in the shell and material in the halo at point $\boldsymbol{x}$.

The mean velocity at point $\boldsymbol{x}$ is used to compute the nine-component, symmetric velocity dispersion tensor σ^{ij}, for the orthogonal directions $\{i, j\} \in \{x, y, z\}$, at the same position $\boldsymbol{x}$:

$$\hat{\sigma}^{ij}(\boldsymbol{x}) = \frac{1}{N_{\rm s}-1}\sum_{n=1}^{N_{\rm s}}\left[v_n^i - \hat{v}^i(\boldsymbol{x})\right]\left[v_n^j - \hat{v}^j(\boldsymbol{x})\right]. \tag{8}$$

The average one-dimensional velocity dispersion $\sigma_{\rm s}^2(\boldsymbol{x})$ is calculated by summing the three eigenvalues $\hat{\sigma}_k^2$ of the velocity dispersion tensor estimated with $\hat{\sigma}^{ij}(\boldsymbol{x})$ (the lengths of the orthogonal axes of the velocity ellipsoid):

$$\widehat{\sigma_{\rm s}^2} = \sum_{k=1}^{3}\hat{\sigma}_k^2\,. \tag{9}$$

We determine $\hat{\sigma}_{\rm s}$ by simply taking the square root. This quantity represents the relative velocity between particles in the shell at point $\boldsymbol{x}$.

Finally, the two components of Γ involving the N-body model are computed using the estimators

$$\hat{\Gamma}_{\rm hs} = \frac{1}{m_{\rm p}}\sum_{V_i\in V} V_i\hat{n}_{{\rm s},i}\rho_{\rm h}(\boldsymbol{x}_i)S(\hat{v}_{\rm s}) \tag{10}$$

and

$$\hat{\Gamma}_{\rm ss} = \sum_{V_i\in V} V_i\,\widehat{n^2}_{{\rm s},i}\;S(\hat{\sigma}_{\rm s}), \tag{11}$$

where the Riemann sum is over the volumes V_i making up the target volume V, and $\hat{n}_i$ and $\widehat{n^2}_i$ are estimated at the centre $\boldsymbol{x}_i$ of each Riemann volume as in Sanderson & Bertschinger (2010). The halo density $\rho_{\rm h}$ is evaluated at the centre of each Riemann volume for consistency with the positional accuracy of the density estimates. Because the Riemann volumes are generally small compared to the gradient of the halo density profile in the regions of interest, the difference between this method of evaluating $\rho_{\rm h}$ and the analytic integral over each pixel used to calculate $\Gamma_{\rm hh}$ should likewise be small.

Recovery of smooth fields from a discrete representation can be sensitive to various discreteness effects, including the choice of smoothing number $N_{\rm s}$ and resolution $N_{\rm p}$ and the local gradient of the density, especially the existence of sharp edges in the distribution. Because of the complexity of the method for determining the velocity dispersion, we used numerical experiments to calculate the bias, variance and rms error of $\sigma_{\rm s}$ for several different values of $N_{\rm s}$, and $N_{\rm p}$ over a range of velocity dispersions. We looked for variations with these parameters, as well as those due to edge effects or density gradient (which is high near the caustic).

For the purposes of the numerical experiments, we define the expectation value of the estimator, $E(\hat{\sigma}_{\rm s})$, as the mean of the estimated values of $\sigma_{\rm s}$ over a given region of the sample:

$$E(\hat{\sigma}_{\rm s}) \equiv \frac{1}{N_{\rm sub}}\sum_{i=1} N_{\rm sub}\hat{\sigma}_{\rm s}(\boldsymbol{x}_i), \tag{12}$$

where $N_{\rm sub}$ is the number of particles falling in that region of the realization and $\boldsymbol{x}_i$ is the position of the ith particle, with $\hat{\sigma}_{\rm s}$ defined as described above. A 'region' could be the entire sample, in which case $N_{\rm sub} = N_{\rm p}$, but we also compared subsets that included and

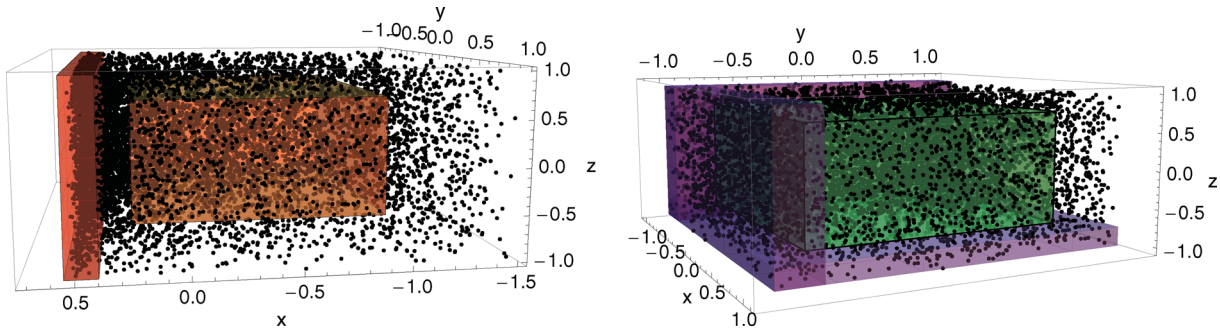

Figure 6. Regions for testing possible edge and density gradient effects in the estimation of the velocity dispersion σ_s. The test compared different regions (edge and centre) in two test distributions: one with a caustic along the x direction (left-hand panel) and one with uniform density (right-hand panel). The edge region in the caustic distribution spanned the caustic surface (red box), while the centre region avoided all the edges and had a small density gradient (orange box). The edge region in the uniform distribution covered all the edges (half are shown in purple), while the central region avoided all of them (green).

excluded edges or caustics. We compared $E(\hat{\sigma}_s)$ to the input value of the velocity dispersion, σ_{in}, by computing the bias $\mathcal{B}$ and variance $\mathcal{V}$ of $E(\hat{\sigma}_s)$, defined as

$$\mathcal{B} \equiv \frac{E(\hat{\sigma}_s)}{\sigma_{in}} - 1 \qquad \text{and} \qquad \mathcal{V} \equiv \frac{1}{N_{sub}\sigma_{in}^2} \sum_{i=1}^{N_{sub}} [\hat{\sigma}_s(\boldsymbol{x}_i) - E(\hat{\sigma}_s)]^2 \ . \tag{13}$$

With these definitions, $\mathcal{B}$ represents the average fractional systematic difference between the input and estimated values of σ_s, and similarly $\mathcal{V}$ measures the average fractional variation of the estimates from their mean (the 'noisiness' of the estimator). The square root of $\mathcal{V}$, often referred to as the standard deviation, is a measure of the spread of all the individual estimates of σ_s.

One can further quantify the performance of the estimator by combining $\mathcal{B}$ and $\mathcal{V}$ in the root-mean-squared (rmse) error defined as

$$(\text{rmse})^2 \equiv \mathcal{B}^2 + \mathcal{V} = \frac{1}{N_{sub}\sigma_{in}^2} \sum_{i=1}^{N_{sub}} [\hat{\sigma}_s(\boldsymbol{x}_i) - \sigma_{in}]^2 \ , \tag{14}$$

which includes both error from a noisy estimator (in $\mathcal{V}$) and error from a biased one (in $\mathcal{B}$). It is important to consider the relative contributions of $\mathcal{B}$ and $\mathcal{V}$ to the rmse, however, so we will discuss all three quantities below.

We calculated the bias, variance and rmse of the expectation values from random realizations of three-dimensional distributions with and without caustics. The realizations were generated at a range of resolutions between $N_p = 10^4$ and 10^5, with the number of particles in a given realization chosen from a Poisson distribution with mean N_p. We used a range of velocity dispersions between 10^{-3} and 10^{-4} and a time unit of 1 to create the caustics. The caustic width is simply $\delta x = \sigma t$ in our map, so this creates caustics with a thickness of 10^{-3}–10^{-4} relative to the units measuring box size as shown in Fig. 6. The same velocity dispersion used in the caustic mapping was also used to assign random velocities to each particle: the velocities were reassigned to caustic particles for consistency with the uniform case, and in order to isolate the effect of density gradients on estimates of the velocity dispersion. The velocity dispersion was calculated at the location of each particle in each sample at $N_s = 10$, 20 and 30.

We tested for edge effects by comparing the estimates of σ_s for two types of test distributions with a uniform velocity dispersion: one with a caustic in it and one with uniform density. The estimator described above was used to estimate σ_s at the location of each particle in a given sample. To test for possible effects of edges and density gradients, we defined two regions in each sample: one near the edge of the distribution and one at the centre of the sample (Fig. 6). The edge region in the caustic distribution is aligned with the caustic surface to probe possible bias from the high density gradient in the caustic, and spans several times the scale width of the caustic. The sizes of the regions are adjusted so they all contain about the same number of particles. The velocity dispersion was estimated at the locations of particles in a given region using *all* particles in the realization. If the edges or density gradient affect the estimation of the velocity dispersion, we expect to see a difference in the bias and/or variance of the estimates for regions near the edges or near the caustic compared to regions that exclude the edges.

To illustrate the effect of edges, we present results for $N_s = 10$ in a pair of realizations with $N_p = 10^5$ (corresponding to $N_{sub} \sim 10^{4.5}$), since these values of N_s, N_p and N_{sub} are appropriate for the N-body realization of M31. We found that the rms error on estimates produced by $\hat{\sigma}_s$ was dominated by the large variance resulting from the low value of N_s and was about 14 per cent in all cases. The bias, which would indicate a systematic error in the estimator, was also independent of the density gradient or the presence of edges in the distribution (Fig. 7). This rms error corresponds to an uncertainty of about 25 per cent in the Sommerfeld coefficient, which is comparable to our uncertainty about the details of the phase-space structure

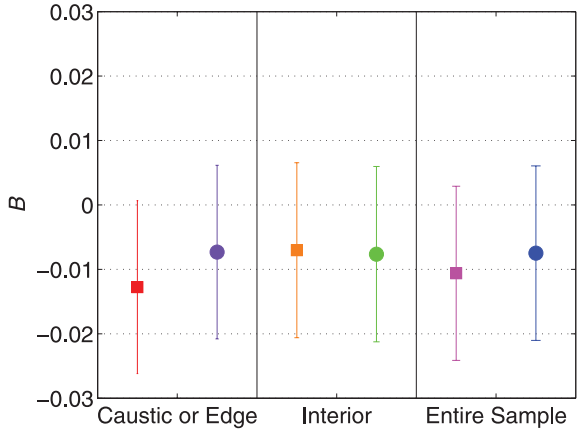

Figure 7. The bias (filled points) and rms error (error bars are one-tenth the rmse) of $E(\hat{\sigma}_s)$ do not appreciably differ between the various regions of the sample, or between the samples as a whole. Print version: squares denote the sample with the caustic; circles denote the uniform density sample. Online: the colours in the figure correspond to the regions depicted in Fig. 6: magenta indicates the entire sample with the caustic and blue indicates the entire uniform density sample.

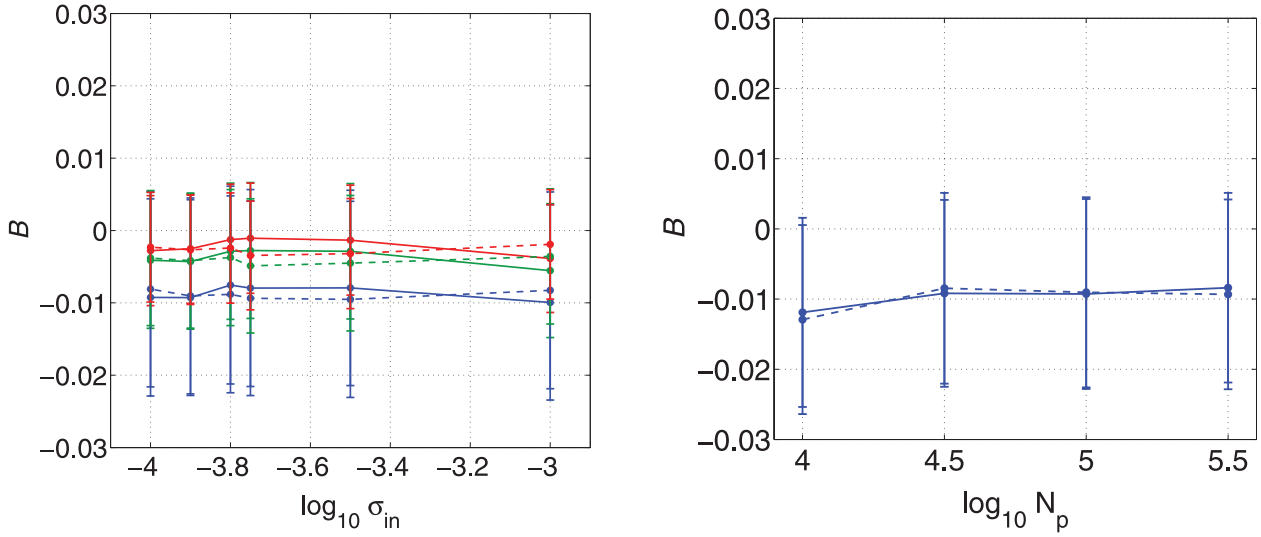

Figure 8. The ability of the estimator to recover velocity dispersions is fairly insensitive to most numerical parameters. The average bias using $N_s = (10, 20, 30)$ is shown in (darkest to lightest grey; blue, green, red, respectively, in the online version) in the left-hand panel, for various input values of σ_{true} in kpc Myr^{-1}. Increasing the smoothing number N_s (left-hand panel) or the resolution N_p (right-hand panel) slightly improves the bias and rms error, regardless of whether the density distribution includes a caustic (solid lines) or is uniform (dashed lines). In the right-hand panel, $N_s = 10$ and N_p is varied; above $\log_{10} N_p = 4.5$ there is not an appreciable difference in the bias. In both panels, the error bars represent one-tenth of the rms error of the estimator.

in this tidal debris and certainly less than the uncertainty about the particle physics model of the dark matter.

The N-body model of the debris uses about 1.3×10^5 particles to represent the entire tidal structure, of which about 4×10^4 end up in Caustic 1 and 2×10^4 end up in Caustic 2. This level of resolution is sufficient to resolve the density distribution of the material if a suitable estimator with a suitably small smoothing number ($N_s = 10$) is used (Sanderson & Bertschinger 2010), but this does not guarantee that the velocity structure of the material is adequately resolved. To maximize the resolution of the velocity structure, we would like to use the smallest possible smoothing number to estimate moments of the velocity distribution as well.

In order to understand how the choice of smoothing number and the resolution of the N-body representation affected the sensitivity of the calculation to small velocity dispersions, we computed the bias and variance for estimates of σ in uniform and caustic density distributions with different input values of the dispersion σ_{true}, at different smoothing numbers N_s, and at varying resolutions N_p. We find that the estimator can reliably estimate velocity dispersions as small as 10^{-4}, with no indication that the bias is dependent on σ (Fig. 8, left-hand panel). If the box size is rescaled to the approximate size of the caustics in the N-body simulation of M31, $\sigma_{in} = 10^{-4}$ corresponds to caustics of width ~ 5 pc, and velocity dispersions of about 5 km s^{-1}. The caustics in M31 have widths closer to 1 kpc, so their density gradient is always many times smaller than those tested though the minimum velocity dispersions are comparable to this limit (Table 1). Choosing a larger N_s does slightly reduce both the bias and the rms error, but will make the estimator less sensitive to small-scale changes in the velocity dispersion. Increasing the resolution also has only a small effect on the bias and virtually none on the rms error (Fig. 8, right-hand panel), which is again dominated by the variance. Based on these tests we conclude that the current level of resolution of the N-body realization and the choice of $N_s = 10$ will recover adequately unbiased estimates of the velocity dispersion, sufficient for the required level of accuracy in this work.

3 BOOST FACTOR

The boost factor is defined as the enhancement over the smooth halo provided by the tidal structure:

$$B \equiv \frac{\Gamma_{hs} + \Gamma_{ss}}{\Gamma_{hh}}. \quad (15)$$

The boost factor is independent of the normalization of S, the branching ratio, and other quantities that are determined by the particular particle physics model of the interaction. Thus, it usefully isolates the effect of the different dependences of the cross-section on velocity without introducing all the complexity of the parameter space of dark matter models. We considered two different power laws for $S(v)$ motivated by previous studies of the Sommerfeld effect (e.g. Arkani-Hamed et al. 2009; Bovy 2009; Lattanzi & Silk 2009; Mardon et al. 2009): $S(v) \propto 1/v$ and $S(v) \propto 1/v^2$. For comparison, we also consider the velocity-independent case $S = 1$.

Both velocity-dependent cases (Fig. 9, middle and right-hand panels) provide a significant, position-dependent enhancement of the tidal structure relative to the background and relative to the velocity-independent case (Fig. 9, left-hand panel). As expected from Fig. 2, the most significant enhancement is at the edges of the two shells and in the stream, where the density is highest and the velocity dispersion is lowest. The enhancement compared to the velocity-independent case is highly non-linear (Fig. 10) because of the correlation between the density and velocity dispersion, which is a product of the phase-space streaming and the radial symmetry of the system's dynamics.

Surprisingly, the tidal stream produces an enhancement that rivals or exceeds that of the shells. In retrospect, examination of the bottom right-hand panel of Fig. 1 and the right-hand panel of Fig. 2 shows that the tidal stream is just as cold as (and perhaps colder than) the shells, its material falling radially inwards in a narrowly collimated and fairly dense band. The tidal stream is fairly dense at radii even larger than the edges of the shells, where the halo is of almost negligible density, leading to an even larger boost factor.

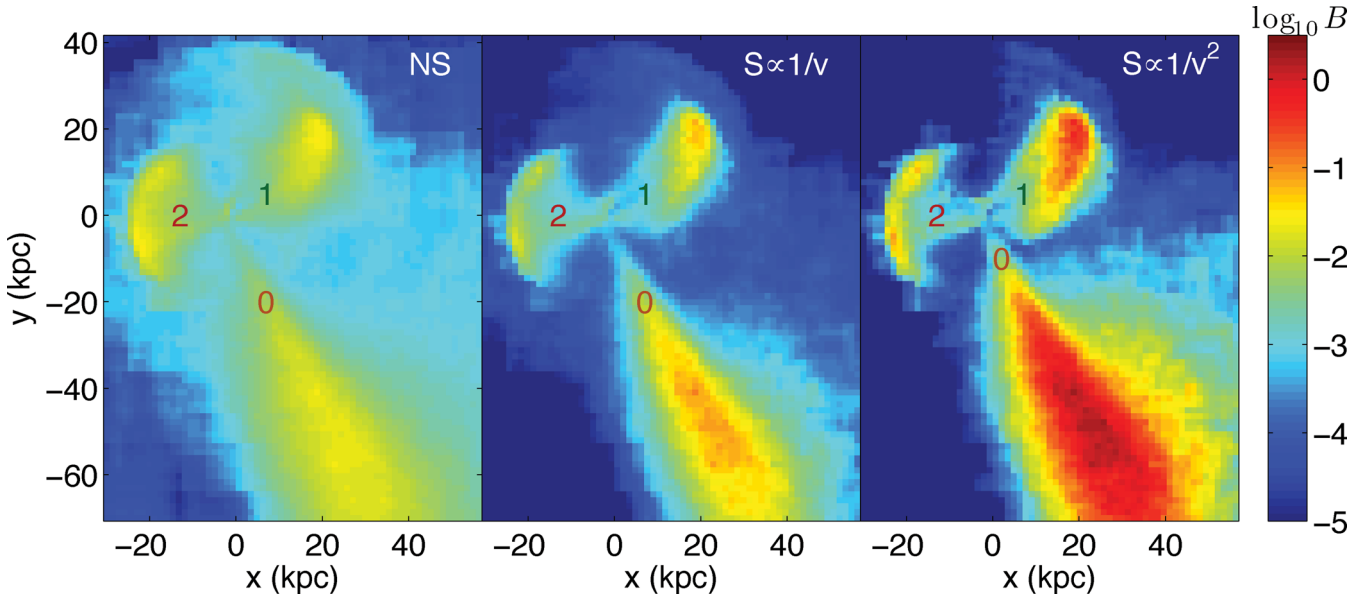

Figure 9. Log of the boost factor (ratio of shell emission to smooth halo emission) for no Sommerfeld enhancement (left-hand panel), $S \propto 1/v$ (middle panel) and $S \propto 1/v^2$ (right-hand panel). The pixel size is chosen to approximate the resolution capability of the *Fermi*-LAT at high energy, as discussed in the text.

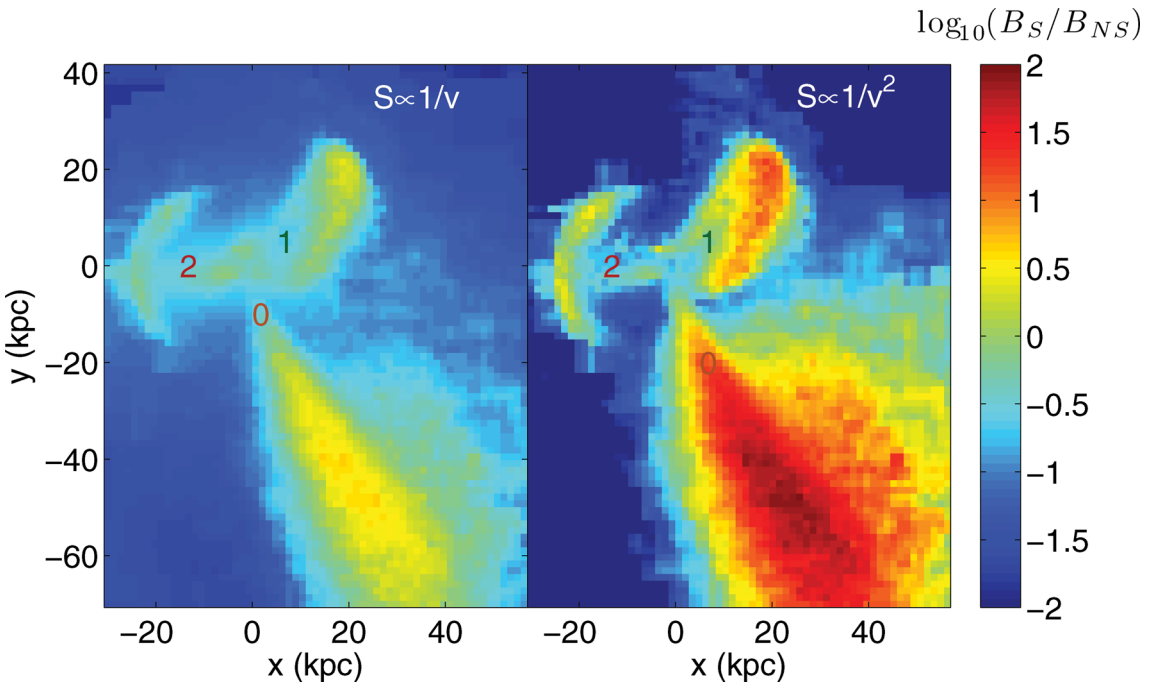

Figure 10. Ratio of the boost for velocity-dependent cross-sections to the boost for velocity-independent cross-sections. The left-hand panel shows the enhancement for $S \propto 1/v$ (in other words, the middle panel of Fig. 9 divided by the left-hand panel) and the right-hand panel shows the enhancement for $S \propto 1/v^2$ (right-hand panel of Fig. 9 divided by the left-hand panel).

Of particular interest is the prediction that if the cross-section to dark matter self-annihilation is proportional to $1/v^2$, then the emission from this tidal structure should be as bright as the background halo at the edges of the shells and in the densest part of the tidal stream. This finding can be used to test the velocity dependence of the dark matter cross-section if the halo of M31 is detected in gamma-rays by *Fermi*. If the halo is detected, Fig. 9 predicts that zeroth-order departures from a smooth emission distribution should be observed if the cross-section depends on $1/v^2$ or higher order, and that these departures should be correlated with the spatial distribution of tidal structures around M31. Likewise, if the cross-section depends on $1/v$, departures should be observed at the 10 per cent level, although this may be beyond the range of current instruments. These predictions are independent of the specific model of the dark matter particle, and are based solely on the assumption of a form for the velocity dependence of the cross-section. If no such departures are observed, the class of models with velocity-dependent cross-sections of that form can be ruled out.

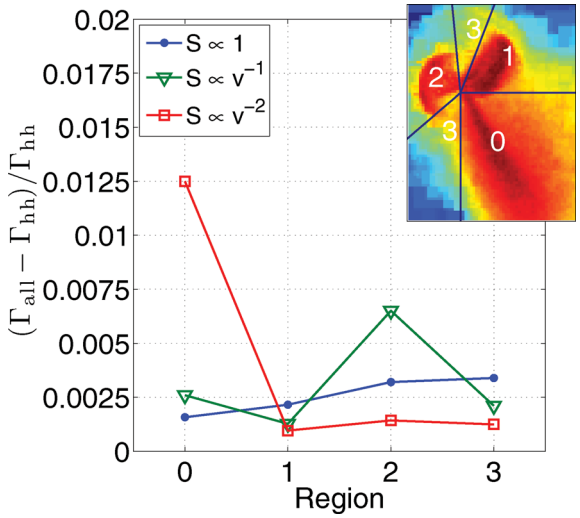

Figure 11. Comparing the boost in different regions can reveal deviations from spherical symmetry in the map, even if the signal from the substructure itself is not fully resolved, for some interaction models. The inset shows the regions over which the sum was calculated.

3.1 Spatial correlations

The particular morphology of the tidal features can significantly improve the chances of a detection for a low signal rate, by correlating the stellar map with the gamma-ray map. Here we demonstrate a coarse version of this by dividing the map into several regions, three centred on a feature and one without significant tidal boosting, and calculating the boost in each of these regions separately (Fig. 11). This coarse contrast method can also allow for slight deviations between the dark matter and stellar distributions, though our calculation assumes perfect tracking. In practice, the boosts would be calculated by fitting a smooth, spherical halo profile to the radially averaged observed distribution of gamma-rays, which does not show much deviation for any of the interaction models we considered, and comparing the observed and fitted signal in each pie-shaped region inspired by the arrangement of the tidal debris, which is highly asymmetric. Including a region assumed to have no boost gives a built-in measurement of the sensitivity of the comparison.

The most prominent feature appears to vary based on the interaction model that is used. For $S \propto 1/v^2$, the tidal tail is the most prominent, deviating from spherical symmetry at the 1 per cent level. For $S \propto 1/v$, the edge-on shell appears at the 0.5 per cent level but the tidal tail is indistinguishable. This is because the cross-term Γ_{hs} is larger than the shell–shell interaction Γ_{ss} for this case, so that the structure at the smallest radius (i.e. largest halo density) is the brightest. Without a velocity-dependent cross-section, none of the features is distinguishable from the background.

4 GAMMA-RAY SIGNAL

In order to determine whether the test described in the previous section could be performed with *Fermi*, we estimated the gamma-ray signal from the halo and tidal substructure for the two forms of $S(v)$ described above. In this section, we discuss the calculation of the signal and its scaling with various parameters.

4.1 Calculation of the signal

We follow the notation of Fornengo, Pieri & Scopel (2004) as adapted by Sanderson & Bertschinger (2010) to calculate the gamma-ray signal, $\mathrm{d}N_\gamma/\mathrm{d}t$, for *Fermi*. As in Fornengo et al. (2004), we separate the dependence on the phase-space distribution of material from most of the details of the dark matter particle model:

$$\Phi_\gamma = \Phi^{\mathrm{C}} \int_{E_{\min}}^{m_\chi} \frac{\mathrm{d}\Phi^{\mathrm{P}}}{\mathrm{d}E_\gamma} A(E_\gamma)\mathrm{d}E_\gamma \mathrm{d}E_\gamma \,. \tag{16}$$

The first term, Φ^{C}, depends only on the mass and velocity distribution of the dark matter and the velocity dependence of the Sommerfeld effect. This term is independent of the energy E_γ of the gamma-rays produced in the interaction:

$$\Phi^{\mathrm{C}} = \frac{1}{4\pi d^2} \int_{\mathrm{pixel}} \mathrm{d}^3\boldsymbol{x}\, \rho^2(\boldsymbol{x}) S[v(\boldsymbol{x})] \,. \tag{17}$$

The signal depends on the distance, d, from M31 and on the local relative velocity v of the dark matter as well as the local mass density ρ. Of course, the rate at which dark matter particles interact with each other really depends on the number density, not the mass density, but since the dark matter mass is model-dependent there is a corresponding factor of $1/m_\chi^2$ in the second term, $\mathrm{d}\Phi^{\mathrm{P}}/\mathrm{d}E_\gamma$, which depends on the particular model of dark matter being used. This term describes the spectrum of gamma-rays produced for a given dark matter model:

$$\frac{\mathrm{d}\Phi^{\mathrm{P}}}{\mathrm{d}E_\gamma} = \frac{\langle\sigma v\rangle_0}{2m_\chi^2} \frac{\mathrm{d}N_\gamma}{\mathrm{d}E_\gamma} \,. \tag{18}$$

The cross-section $\langle\sigma v\rangle_0$ denotes the value of the cross-section without Sommerfeld enhancement. $\mathrm{d}N_\gamma/\mathrm{d}E_\gamma$ is the spectrum of gamma-rays produced in a particular dark matter model.

The total signal in a given detector, $\mathrm{d}N_\gamma/\mathrm{d}t$, is calculated by integrating the spectrum of observed radiation over the energy range of the detector, weighted by the effective area for the detector A_{eff}; the only other detector-dependent piece is the lower limit of the integral $E_{\min}$, the threshold energy for the detection of gamma-rays, chosen to be 100 MeV for consistency with the *Fermi* sensitivity range. (The upper limit of the integral is simply the dark matter mass, as required by energy conservation.) For the *Fermi*-LAT, whose effective area is roughly energy-independent above 1 GeV (Rando 2009), we can calculate the flux Φ_γ independent of the effective area, since we are interested mainly in determining whether the structure is above the detection threshold.

With this simplification, we find that Φ^{P} is simply proportional to the total yield $N_\gamma(E_{\min})$ above $E_{\min}$, so that

$$\Phi^{\mathrm{P}}(E_{\min}) = \frac{\langle\sigma v\rangle_0}{2m_\chi^2} N_\gamma(E_{\min}). \tag{19}$$

4.1.1 *Sommerfeld enhancement*

Arkani-Hamed et al. (2009), Lattanzi & Silk (2009) and others have shown that the Sommerfeld interaction can be easily modelled as a Yukawa force with coupling constant α and a mediating particle mass m_1. In this analogy, the solution to the radial Schrodinger equation with a Yukawa potential exhibits two characteristic behaviours of the cross-section enhancement $S \equiv \langle\sigma v\rangle/\langle\sigma v\rangle_0$. At very low relative speeds, for resonant values of the mass ratio m_χ/m_1, S is proportional to the inverse square of the relative speed:

$$S^{\mathrm{res}} = \left(\frac{\beta^*}{\beta}\right)^2 , \tag{20}$$

where $\beta = v/c$ is the relative velocity of dark matter particles. A 'low' relative speed is small compared to the characteristic velocity

$$\beta^* = \sqrt{\frac{\alpha m_1}{m_\chi}}. \tag{21}$$

Previous work on the Sommerfeld effect has proposed values of around 10^{-2} for the coupling constant α, and a wide range of m_χ and m_1. We choose $\alpha = 1/30$ for this work, noting that the enhancement only depends on the quantity β^* and may thereby be rescaled to any combination of $\alpha m_1/m_\chi$. The first resonant peak occurs when $m_1/m_\chi \sim 0.2$ (Lattanzi & Silk 2009).

The N-body realization gives velocities in units of kpc Myr^{-1} and hence introducing appropriate units and values leads to the expression

$$S^{\rm res} = S_0^{\rm res}\left(\frac{v}{\rm kpc\,Myr^{-1}}\right)^{-2}\left(\frac{\alpha}{10^{-2}}\right)\left(\frac{m_1/m_\chi}{10^{-2}}\right), \tag{22}$$

where $S_0^{\rm res} = 9.4$.

Away from resonance, the enhancement takes on the form

$$S^{\rm nr} = \frac{\pi\alpha}{\beta} = S_0^{\rm nr}\left(\frac{v}{\rm kpc\,Myr^{-1}}\right)^{-2}\left(\frac{\alpha}{10^{-2}}\right), \tag{23}$$

where $S_0^{\rm nr} = 9.6$. This form is also valid at intermediate values of β between β^* and α.

4.1.2 Phase-space distribution factor

With an N-body realization, the integral in equation (17) is calculated in terms of the number density n for N-body particles of mass $m_{\rm p}$, so that

$$\Phi^{\rm C} = \frac{S_0^{\rm res} m_{\rm p}^2}{4\pi d^2}\left(\frac{\alpha}{10^{-2}}\right)\left(\frac{m_1/m_\chi}{10^{-2}}\right)\int {\rm d}^3\boldsymbol{x}\; n^2(\boldsymbol{x})\left[\frac{v(\boldsymbol{x})}{\rm kpc\;\;Myr^{-1}}\right]^{-2} \tag{24}$$

for the resonant interaction and similarly for the non-resonant regime. The number density n is likewise in units of kpc^{-3} and the volume element ${\rm d}^3\boldsymbol{x}$ in units of kpc^3 and hence the result of the numerical integration returned by the density estimator is

$$\frac{\Gamma^{v^2}}{\rm kpc^{-5}\,Myr^2} \equiv \int\left(\frac{{\rm d}^3\boldsymbol{x}}{\rm kpc^3}\right)\left[\frac{n^2(\boldsymbol{x})}{\rm kpc^{-6}}\right]\left[\frac{v(\boldsymbol{x})}{\rm kpc\,Myr^{-1}}\right]^{-2} \tag{25}$$

on resonance and

$$\frac{\Gamma^{v}}{\rm kpc^{-4}\,Myr} \equiv \int\left(\frac{{\rm d}^3\boldsymbol{x}}{\rm kpc^3}\right)\left[\frac{n^2(\boldsymbol{x})}{\rm kpc^{-6}}\right]\left[\frac{v(\boldsymbol{x})}{\rm kpc\,Myr^{-1}}\right]^{-1} \tag{26}$$

off resonance.

Using the distance $d = 785$ kpc from M31 and the particle mass $m_{\rm p} \sim 10^4\,{\rm M}_\odot$ from the N-body simulation, and converting to standard units for the quantity $\Phi^{\rm C}$, we obtain the phase-space-dependent factor

$$\Phi^{\rm C,res} = \Phi_0^{\rm C,res}\left(\frac{d}{785\,\rm kpc}\right)^{-2}\left(\frac{\alpha}{10^{-2}}\right)\left(\frac{m_1/m_\chi}{10^{-2}}\right) \times\left(\frac{m_{\rm p}}{10^4\,{\rm M}_\odot}\right)^2\left(\frac{\Gamma^{v^2}}{\rm kpc^{-5}\,Myr^2}\right), \tag{27}$$

where $\Phi_0^{\rm C,res} = 1.75\times10^{-13}\,{\rm GeV^2\,kpc\,cm^{-6}}$, for the resonant interaction and

$$\Phi^{\rm C,nr} = \Phi_0^{\rm C,nr}\left(\frac{d}{785\,\rm kpc}\right)^{-2}\left(\frac{\alpha}{10^{-2}}\right) \times\left(\frac{m_{\rm p}}{10^4\,{\rm M}_\odot}\right)^2\left(\frac{\Gamma^{v}}{\rm kpc^{-4}\,Myr}\right), \tag{28}$$

where $\Phi_0^{\rm C,nr} = 1.79\times10^{-13}\,{\rm GeV^2\,kpc\,cm^{-6}}$, for the non-resonant interaction.

4.1.3 Particle physics factor

The particle physics factor in the flux can be written as

$$\Phi^{\rm P}(E_{\rm min}) = \Phi_0^{\rm P} N_\gamma(E_{\rm min})\left(\frac{\langle\sigma v\rangle_0}{3\times10^{-26}\,\rm cm^3\,s^{-1}}\right)\left(\frac{m_\chi}{10\,\rm GeV}\right)^{-2}, \tag{29}$$

where $\Phi_0^{\rm P} = 4.63\times10^{-7}\,{\rm cm^4\,kpc^{-1}\,GeV^{-2}\,s^{-1}}$. The gamma-ray yield N_γ is usually of the order of 1 per annihilation or less, depending on the dark matter model (Mardon et al. 2009).

4.1.4 Complete expression

Combining equation (27) or (28) with equation (29) gives the master equation for Φ_γ including all the scalings:

$$\Phi_\gamma^{\rm res} = 8.1\times10^{-20} N_\gamma\,{\rm cm^{-2}\,s^{-1}}\left(\frac{m_\chi}{10\,\rm GeV}\right)^{-2} \times\left(\frac{m_1/m_\chi}{10^{-2}}\right)\left(\frac{\alpha}{10^{-2}}\right)\left(\frac{\langle\sigma v\rangle_0}{3\times10^{-26}\,\rm cm^3\,s^{-1}}\right) \times\left(\frac{m_{\rm p}}{10^4\,{\rm M}_\odot}\right)^2\left(\frac{d}{785\,\rm kpc}\right)^{-2}\left(\frac{E(\hat\Gamma^{v^2})}{\rm kpc^{-5}\,Myr^2}\right) \tag{30}$$

for the resonant process, and

$$\Phi_\gamma^{\rm nr} = 8.3\times10^{-20} N_\gamma\,{\rm cm^{-2}\,s^{-1}}\left(\frac{m_\chi}{10\,\rm GeV}\right)^{-2} \times\left(\frac{\alpha}{10^{-2}}\right)\left(\frac{\langle\sigma v\rangle_0}{3\times10^{-26}\,\rm cm^3\,s^{-1}}\right) \times\left(\frac{m_{\rm p}}{10^4\,{\rm M}_\odot}\right)^2\left(\frac{d}{785\,\rm kpc}\right)^{-2}\left(\frac{E(\hat\Gamma^{v})}{\rm kpc^{-4}\,Myr}\right) \tag{31}$$

for the non-resonant process. The comparable expression without the Sommerfeld boost is (Sanderson & Bertschinger 2010)

$$\Phi_\gamma^{\rm NS} = 9.6\times10^{-22} N_\gamma\,{\rm cm^{-2}\,s^{-1}} \times\left(\frac{m_\chi}{10\,\rm GeV}\right)^{-2}\left(\frac{\langle\sigma v\rangle_0}{3\times10^{-26}\,\rm cm^3\,s^{-1}}\right) \times\left(\frac{m_{\rm p}}{10^4\,{\rm M}_\odot}\right)^2\left(\frac{d}{785\,\rm kpc}\right)^{-2}\left(\frac{E(\hat\Gamma_{\rm NS})}{\rm kpc^{-3}}\right). \tag{32}$$

4.2 Results for the *Fermi* band

Using equations (30), (31) and (32), we produce maps of the total flux Φ_γ in gamma-rays in the *Fermi* band, including both the halo and the substructure, for several scenarios. Fig. 12 compares the results for resonant, non-resonant and non-Sommerfeld cases for two different choices of m_χ: 10 GeV and 1 TeV. The former is optimistic but realistic for models with no Sommerfeld boost; the latter is characteristic for models with a Sommerfeld boost. We include results at 10 GeV for Sommerfeld-like boosts for completeness, although a particle model for such an enhancement at low m_χ does not exist to our knowledge. However, we do note that Slatyer et al. (2011) point out that mediating particles with masses even lower than a few GeV (the lowest considered here) cannot be ruled out by current measurements, given the uncertainty about the distribution of substructure in the Galaxy, so this panel may yet be relevant.

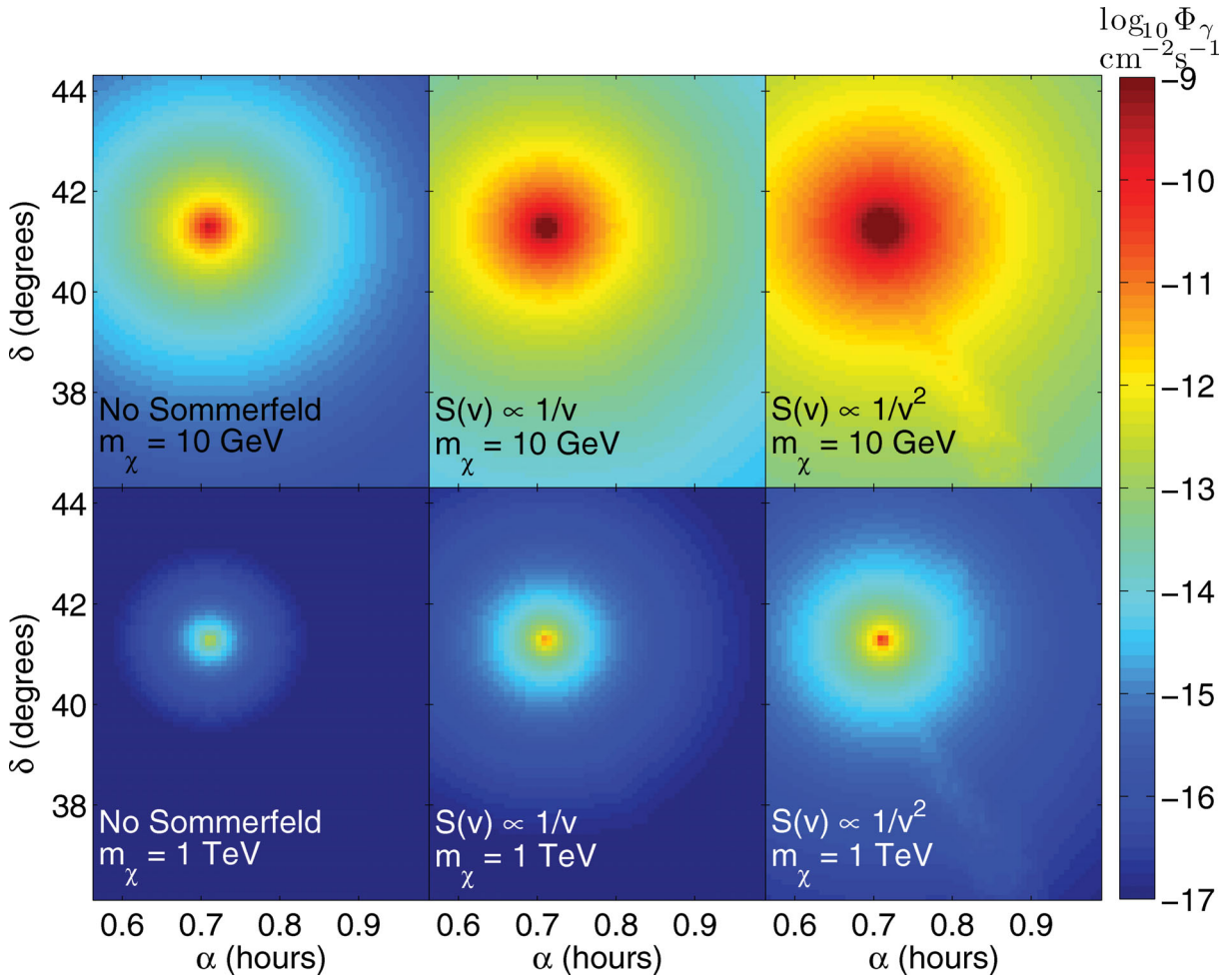

Figure 12. Logarithmic map of predicted gamma-ray flux in the *Fermi* band ($E_\gamma > 100$ MeV) for various models of the dark matter interaction. The label 'no Sommerfeld' indicates direct annihilation to standard-model particles without an intermediate step. We consider the low-mass case $m_\chi = 10$ GeV with a Sommerfeld-like boost for comparison, even though the standard mechanism for Sommerfeld enhancement is invalid for such a low dark matter mass. We also take a typical case for Sommerfeld enhancement with $m_\chi = 1$ TeV.

The case $S \propto 1/v$ is brighter than $S = 1$, but only the halo is visible in both cases: the tidal features are below the smooth emission by several orders of magnitude. In Table 2, we see that the cross-interaction signal $\Phi_{\rm hs}$ is larger than the signal $\Phi_{\rm ss}$ from interactions within the debris, so that overall the signal from the substructure scales only linearly with the substructure density at leading order. However, the structure may still be marginally detectable using the coarser test described in Section 3.1, given sufficient sensitivity to detect the halo at appropriate radii.

In the case where $S \propto 1/v^2$, the enhancement is non-linear enough in both ρ and σ that although the centre of the halo is still the brightest part of the structure, the tidal features stand out above the halo at their radii. Table 2 shows that in this case $\Phi_{\rm ss} > \Phi_{\rm hs}$, indicating that for this case the leading-order signal really scales with the square of the substructure density. This structure is still at least an order of magnitude below *Fermi*'s current sensitivity regime, but if such a sensitivity were achieved, a search for deviations from spherical symmetry in the gamma-ray emission would be able to test the velocity dependence of the interaction cross-section.

We also note that the values of $\Phi_{\rm hh}$ in the table depend primarily on the inner slope of the mass profile as discussed in Section 2, so the fact that they exceed the measured signal from M31 is merely a reflection of the uncertainty of this parameter.

Table 2. Total flux from the halo and tidal structure, compared to the recent *Fermi* detection of M31.

Source	$\Phi_\gamma, m_\chi = 10$ GeV (cm^{-2} s^{-1})	$\Phi_\gamma, m_\chi = 1$ TeV (cm^{-2} s^{-1})
$\Phi_{\rm hh}^{\rm NS}$	1.6×10^{-9}	1.1×10^{-12}
$\Phi_{\rm hs}^{\rm NS}$	3.8×10^{-12}	2.7×10^{-15}
$\Phi_{\rm ss}^{\rm NS}$	4.8×10^{-14}	3.4×10^{-17}
$\Phi_{\rm hh}^{\rm nr}$	5.0×10^{-8}	2.4×10^{-11}
$\Phi_{\rm hs}^{\rm nr}$	8.2×10^{-11}	4.0×10^{-14}
$\Phi_{\rm ss}^{\rm nr}$	5.8×10^{-12}	2.8×10^{-15}
$\Phi_{\rm hh}^{\rm res}$	2.9×10^{-7}	1.4×10^{-10}
$\Phi_{\rm hs}^{\rm res}$	1.5×10^{-10}	7.2×10^{-14}
$\Phi_{\rm ss}^{\rm res}$	2.8×10^{-10}	1.4×10^{-13}
$\Phi_{\rm M31}$[a]	9×10^{-9}	

[a] Fermi LAT Collaboration (2010).

5 DISCUSSION

Thanks to their low velocity dispersion and relatively high density, cold tidal streams and young caustics can provide a significant boost

to the dark matter self-annihilation rate if the cross-section is non-linearly dependent on the relative velocity, as in the Sommerfeld scenario. The particular morphology of tidal streams, their location far from the centres of galaxies, and the apparent tracking of the stellar and dark components also make these features an attractive place to search for an annihilation signal, as the correlation with the stellar shape makes it easier to differentiate such a signal from a smooth halo distribution. In fact, at distances typical of tidal debris 30–50 per cent of the halo's mass may be in streams (Maciejewski et al. 2010; Wang et al. 2011).

In this work, we computed the boost to a smooth background from tidal substructure observed in star-count maps of the Andromeda galaxy for two different velocity-dependent cross-sections proposed for Sommerfeld-type annihilations between weakly interacting, massive dark matter particles (in which a light helper particle forms in an intermediate state between the dark matter annihilation and the production of standard-model particles). We used an existing *N*-body model of the structure to estimate the density and relative velocity of the material in the substructure with suitably unbiased algorithms and a reasonable choice of numerical parameters. We found that in both cases the emission from the tidal structure could locally boost the annihilation emission by up to factors of 5. The case where the cross-section $\langle \sigma v \rangle \propto 1/v^2$ produced a boost large enough for the signal from the tidal structure to outshine the smooth halo at large radii, though the estimated signal is several orders of magnitude below the current *Fermi* sensitivity for reasonable choices of the dark matter parameters. However, if an instrument with the required sensitivity existed, a search for emission from the tidal substructure would constitute a test of the velocity dependence of the dark matter cross-section, since only in the $1/v^2$ case is the tidal structure visible.

6 FUTURE WORK

One intriguing result of this work is that tidal streams that are sufficiently massive and collimated (i.e. young and/or cold) can produce significant local boosts of the annihilation signal if the cross-section is velocity-dependent. Such streams could be a significant contributor to the gamma-ray luminosity of the outer regions of haloes in the Sommerfeld scenario, especially if cosmological simulations accurately predict the percentage of streams. State-of-the-art cosmological simulations of individual galactic haloes can resolve this coarse-grained phase-space structure, and could be used to estimate this contribution.

Low-frequency radio observations could also be used to search for signals from dark matter in tidal substructures, via channels that produce high-energy electrons which then give rise to synchrotron radiation through interactions with the galactic magnetic field. A map of the polarization must be correlated with the observed stellar stream, under the assumption that the dark matter and stars track each other, to search for such a signal (Zaroubi, private communication). In future work, we will consider whether this channel could produce a signal detectable with a low-frequency array such as LOFAR, either in M31 or in high-latitude streams in our own Galaxy.

ACKNOWLEDGMENTS

The work for this paper was done during a research stay at the Institut d'Astrophysique de Paris by RES, who thanks the Institut for their gracious hospitality. RM thanks French ANR OTARIE for support.

REFERENCES

Arkani-Hamed N., Finkbeiner D. P., Slatyer T. R., Weiner N., 2009, Phys. Rev. D, 79, 015014
Bertschinger E., 1985, ApJS, 58, 39
Borriello E., Cuoco A., Miele G., 2009, ApJ, 699, L59
Bovy J., 2009, Phys. Rev. D, 79, 083539
Cirelli M., Cline J. M., 2010, Phys. Rev. D, 82, 023503
Fardal M. A., Babul A., Geehan J. J., Guhathakurta P., 2006, MNRAS, 366, 1012
Fardal M. A., Guhathakurta P., Babul A., McConnachie A. W., 2007, MNRAS, 380, 15
Rando R. (Fermi LAT Collaboration), 2009, preprint (arXiv:0907.0626)
Fermi LAT Collaboration, 2010, A&A, 523, L2
Fornengo N., Pieri L., Scopel S., 2004, Phys. Rev. D, 70, 103529
Galli S., Iocco F., Bertone G., Melchiorri A., 2009, Phys. Rev. D, 80, 023505
Geehan J. J., Fardal M. A., Babul A., Guhathakurta P., 2006, MNRAS, 366, 996
Ibata R., Irwin M., Lewis G., Ferguson A. M. N., Tanvir N., 2001, Nat, 412, 49
Lattanzi M., Silk J., 2009, Phys. Rev. D, 79, 083523
McConnachie A. W. et al., 2009, Nat, 461, 66
Maciejewski M., Vogelsberger M., White S. D. M., Springel V., 2010, MNRAS, 415, 2475
March-Russell J., West S. M., 2009, Phys. Lett. B, 676, 133
Mardon J., Nomura Y., Stolarski D., Thaler J., 2009, J. Cosmol. Astropart. Phys., 5, 16
Mohayaee R., Shandarin S. F., 2006, MNRAS, 366, 1217
Navarro J. F., Frenk C. S., White S. D. M., 1996, ApJ, 462, 563
Navarro J. F. et al., 2010, MNRAS, 402, 21
Peñarrubia J., Navarro J. F., McConnachie A. W., 2008a, ApJ, 672, 904
Peñarrubia J., Navarro J. F., McConnachie A. W., 2008b, Astron. Nachr., 329, 934
Peñarrubia J., Navarro J. F., McConnachie A. W., 2008c, ApJ, 673, 226
Robertson B. E., Zentner A. R., 2009, Phys. Rev. D, 79, 083525
Sanderson R. E., Bertschinger E., 2010, ApJ, 725, 1652
Slatyer T. R., Toro N., Weiner N., 2011, preprint (arxiv :1107.3546)
Wang J. et al., 2011, MNRAS, 413, 1373

This paper has been typeset from a TEX/LATEX file prepared by the author.